The effect of carrier gas flow rate on the growth and optical properties of MoS_2 nanosheets by chemical vapor deposition

ZUSONG ZHU*, JIANCUN YOU
School of Electronic Engineering and Intelligent Manufacturing, Anqing Normal University, Anqing 246133, People's Republic of China

The effect of carrier gas flow rate on the growth and optical properties of molybdenum disulfide (MoS_2) layers grown on SiO_2/Si substrates by atmospheric pressure chemical vapor deposition (CVD) with MoO_3 and S powder as the precursors was investigated. Optical microscopy, Raman and photoluminescence measurements indicate that carrier gas flow rate plays a crucial role in the growth and optoelectrical properties of MoS_2 nanosheets. The regular triangular MoS_2 monolayer with best crystalline quality and large edge sides is synthesized at the carrier gas flow rate about 75sccm.

(Received June 21, 2024; accepted August 5, 2025)

Keywords: MoS_2, Chemical vapor deposition, Carrier gas flow rate, Crystalline quality

1. Introduction

Monolayer molybdenum disulfide (MoS_2) has attracted increasing attention in recent years due to its special structure and excellent physical properties [1-3]. Preliminary researches demonstrated that MoS_2 has many promising application prospects in optoelectronic devices [4-6], field effect transistors [7,8], flexible electronics [9], electrocatalysis [10-12], and so on. Therefore, it is vital to develop a reliable and reproducible synthesis technology of monolayer MoS_2 with good crystalline quality and large-area uniformity.

Some successes have been achieved in the synthesis of MoS_2 nanosheets by adopting synthesis techniques such as mechanical exfoliation [13], chemical vapor deposition (CVD)[14-17], magnetron sputtering [18], atomic layer deposition [19] and hydrothermal synthesis [20]. Among these aforementioned synthesis methods, CVD is the most promising method of synthesizing good crystalline quality and large-area uniformity MoS_2 nanosheets due to its advantages including reproducible synthesis, high purity and lower cost. And some strategies [21-24] have been proposed for modifying traditional CVD, including plasma-enhanced CVD, microcavity-based CVD, vertical CVD, low pressure CVD, separated supply of precursors at different flow rates, and the use of perylene-3,4,9,10-tetracarboxylic acid tetrapotassium salt (PTAS) seeding promoters for growing large area, even wafer-scale, and high quality MoS_2 nanosheets. Recent researches [25-28] have shown that the characteristics of MoS_2 nanosheets such as morphology, crystalline quality, lateral size, number of layers and defects are significantly affected by the synthesis parameters including growth temperature, carrier gas flow rate, pressure, precursor source, type of substrate. Carrier gas flow rate is one of the important parameters on the MoS_2 growth because of its prominent roles in the dilution of the gaseous precursors (MoO_3 and S), delivering reactants to the reaction zone and driving by-products out of the CVD system. Cao et al. [29] and Liu et al. [26] investigated the effect of Ar carrier gas flow rates (5-35sccm; 30 and 100sccm, respectively) on the morphology and lateral size of MoS_2 synthesized by solid MoO_3 and S powders. Esposito et al. [30] demonstrated that N_2 carrier gas flow rates (150-300 sccm) can modify the structure and morphology of multi-apex triangular MoS_2 grown using a liquid molybdenum precursor. However, the effect of N_2 carrier gas flow rate on the growth and optoelectrical properties of MoS_2 nanosheets synthesized from solid MoO_3 and S powders remains unexplored.

In this paper, monolayer MoS_2 nanosheets were synthesized by CVD on SiO_2/Si substrate at different carrier gas (N_2) flow rate of 50sccm, 75sccm, 100sccm, 150sccm and 200sccm. The correlation between the carrier gas flow rate and the morphology and optical properties of as-grown MoS_2 nanosheets was systematically investigated.

2. Experimental sections

A single temperature zone furnace with an additional heating ring was used for the synthesis of MoS_2 nanosheets. The schematic of the CVD system is shown in Fig. 1. The cylindrical quartz tube is 80mm in diameter and 1400mm in length. 120mg S powder (Alfa Aesar, 99.999%) and 30mg MoO_3 powder (99.95%) putting in two separate quartz boats were placed in the center of the upstream heating ring and downstream intrinsic furnace respectively. To avoid S vapor from reacting with MoO_3

before reaching the reaction zone, the distance of the two quartz boats is about 16cm. Si wafers covered with a 300 nm thick SiO_2 layer were used as substrates. The substrate was placed face-down above the MoO_3 power. High purity N_2 was used as carrier gas. The quartz tube was purged by N_2 for 30min with the flow rate of 500sccm to remove hosting gases. Then the furnace temperature was raised up to 100℃ in 5min and maintained at this temperature for 30min with 500sccm N_2. Afterwards, the furnace temperature was increased from 100℃ to 700℃ in 40min and remained for 30min (growth time). In order to investigate the effect of carrier gas flow rate, the growth processes were implemented at different flow rates of 50, 75, 100, 150 and 200sccm. The S powder was heated up to 190℃ simultaneously when the furnace temperature reached 700℃. And then the furnace temperature was decreased to 580℃ in 15min. Finally, the furnace was cooled down to room temperature naturally under the N_2 flow rate of 500sccm to purge the excess reactants out of the furnace and to avoid the growth of intermediate products such as $MoOS_2$ and MoO_{3-x}.

The morphology of the as-grown MoS_2 nanosheets was examined by Olympus BX41RF-LED optical microscope. Raman spectra were recorded by Renishaw in Via spectrometer with exciting laser at 514nm wavelength. The exciting laser was focused on MoS_2 nanosheets with the 50× objective lens. The photoluminescence (PL) spectra were collected by the same Raman microscopic system by using PL mode.

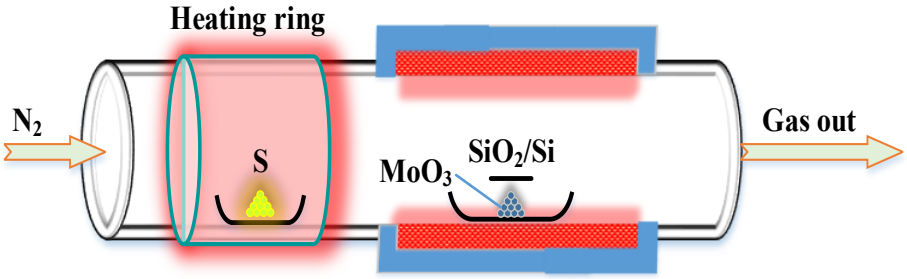

Fig. 1. Schematic illustration of the MoS_2 nanosheets CVD synthesis system (colour online)

3. Results and discussion

3.1. Optical microscopy

Fig. 2 shows optical microscopy images of the MoS_2 nanosheets for increasing carrier gas flow rates. As shown in Fig. 2, the morphology of MoS_2 nanosheets relies strongly on carrier gas flow rates in the range of 50~150sccm. At a low flow rate of 50sccm, a great deal of isolated monolayer equilateral triangle MoS_2 nanosheets with sharp edges and average edge length of 20μm can be observed on the substrate (Fig.2a). When the flow rate is increased to 75sccm, a large amount of individual perfect triangular MoS_2 nanosheets distribute on the substrate and the edge length increases to between 25 and 45μm (Fig. 2b). With further increasing flow rate to 100sccm, the distribution density of MoS_2 nanosheets is larger but the coalescence phenomenon occurs between MoS_2 nanosheets (Fig.2c). Nevertheless, as the flow rate rose to 150sccm, the coverage and size of MoS_2 nanosheets decrease significantly, with an average size of about 10μm. Meanwhile, the morphology of MoS_2 nanosheets changes to three-point star shapes (Fig.2d). If the flow rate continues to enhance to 200sccm, the morphology and the size of MoS_2 nanosheets are similar to those of 150sccm. However, MoS_2 nanosheets distributed sparsely on the substrate. Therefore, the morphology and size of MoS_2 nanosheets can be effectively regulated by the control of the carrier gas flow rate.

The morphology evolution of as-grown MoS_2 nanosheets with the carrier gas flow rate can be estimated qualitatively as follows. It should be first realized CVD deposition process, such as evaporation of precursors (MoO_3 and S), diffusion of precursor vapors driven by N_2 carrier gas, adsorption of the precursors and deposition reaction on the substrate surface. In our experiment, the source temperature and substrate temperature are unchanged. Therefore, the evaporation rate of precursors can be assumed at a constant value even though the flow rate has changed. Obviously, the precursor vapor diffusion rate increases with the increase of the carrier gas flow rate. It is noticeable that the amount of S vapor near the substrate depends mainly on the carrier gas flow rate, while the amount of MoO_3 vapor relied mostly on the evaporation rate of MoO_3 source rather than the carrier gas flow rate because the substrate is directly above MoO_3 source (Fig.1). However, the gas residence time $\tau = \frac{P_i T_o V}{P_o T_i F}$ is shortened with the increase of the carrier gas flow rate. τ is the gas residence time, P_i and T_i are the pressure and temperature inside the furnace, P_o and T_o are the environmental pressure and temperature outside the furnace, V is the volume of the quartz tube and F is the carrier gas flow rate. When the carrier gas flow rate is lower than 100sccm, the S vapor diffusion rate is relatively small, resulting in only a smaller amount of S precursor being transported to the vicinity of the substrate. The Mo-rich growth environment and long residence time of the precursor vapors are more likely to grow regular triangular morphology MoS_2 with sharp and straight edges (Fig.2a, b and c). Besides, due to the long residence time of precursor vapor, the MoO_3 and S can react sufficiently. The size of MoS_2 nanosheets is larger than that under a high flow rate. When the carrier gas flow rate is higher

than 100sccm, for example, 150sccm or 200sccm, the S vapor diffusion rate is relatively large, resulting in a larger amount S being carried to the reaction zone. The S-rich environment will suppress the further volatilization of MoO_3 powder, leading to the formation of MoS_2 sheets with three-point star shapes. Meantime the coverage and size of MoS_2 decrease with increasing flow rate due to insufficient reaction between MoO_3 and S in the short residence time.

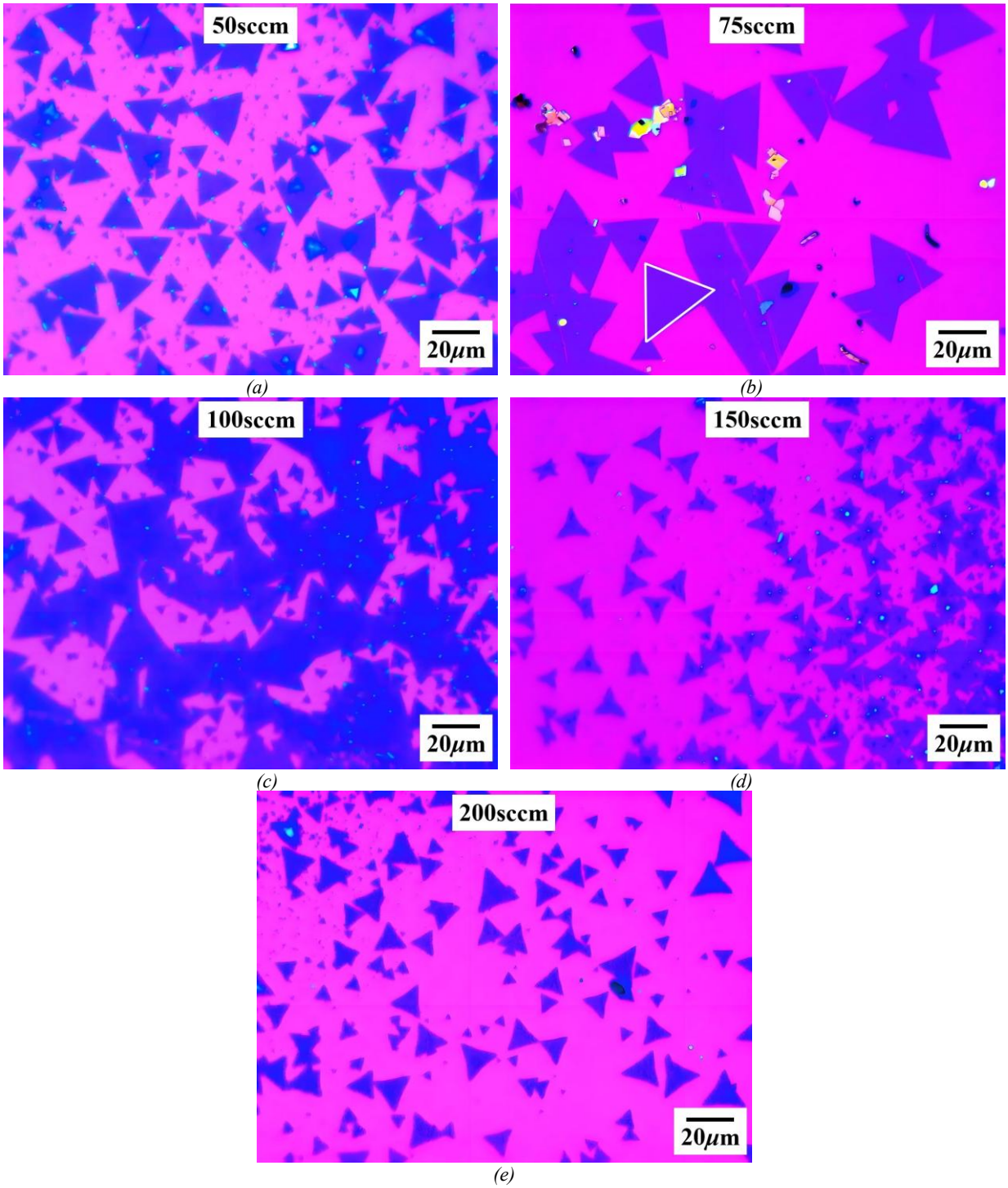

Fig. 2. Optical images of MoS_2 nanosheets with different carrier gas flow rates. (a) 50sccm, (b) 75sccm, (c) 100sccm, (d) 150sccm, (e) 200sccm (colour online)

3.2. Raman spectra

Raman spectroscopy is one of the most effective tools for the characterization of few-layer MoS_2. For monolayer MoS_2, the Raman band appearing in the 382-385cm^{-1} spectral region is known as E^1_{2g} vibration mode and the one appearing in the 402-404 cm^{-1} region of the wavenumber is attributed to A_{1g} vibration mode. Raman spectrum of the as-grown MoS_2 nanosheets with different gas flow rates is shown in Fig. 3a. In this study, there are two main peaks in the spectrum. The obviously E^1_{2g} and A_{1g} peaks are presented at 383.4~385.1cm^{-1} and 401.7~403.6cm^{-1}, respectively. The A_{1g} Raman mode exhibits a red shift compared to that previously reported, resulting from n-type doping of MoS_2 [31]. The peak intensity ratio of E^1_{2g} and A_{1g} is detected as a rough estimate of MoS_2 crystallization quality [32]. In the current study, the intensity ratio of E^1_{2g} and A_{1g} peak is more than four for gas flow rates of 75 sccm, which indicates that the as-grown MoS_2 has a better crystalline structure than the samples of the other gas flow rates.

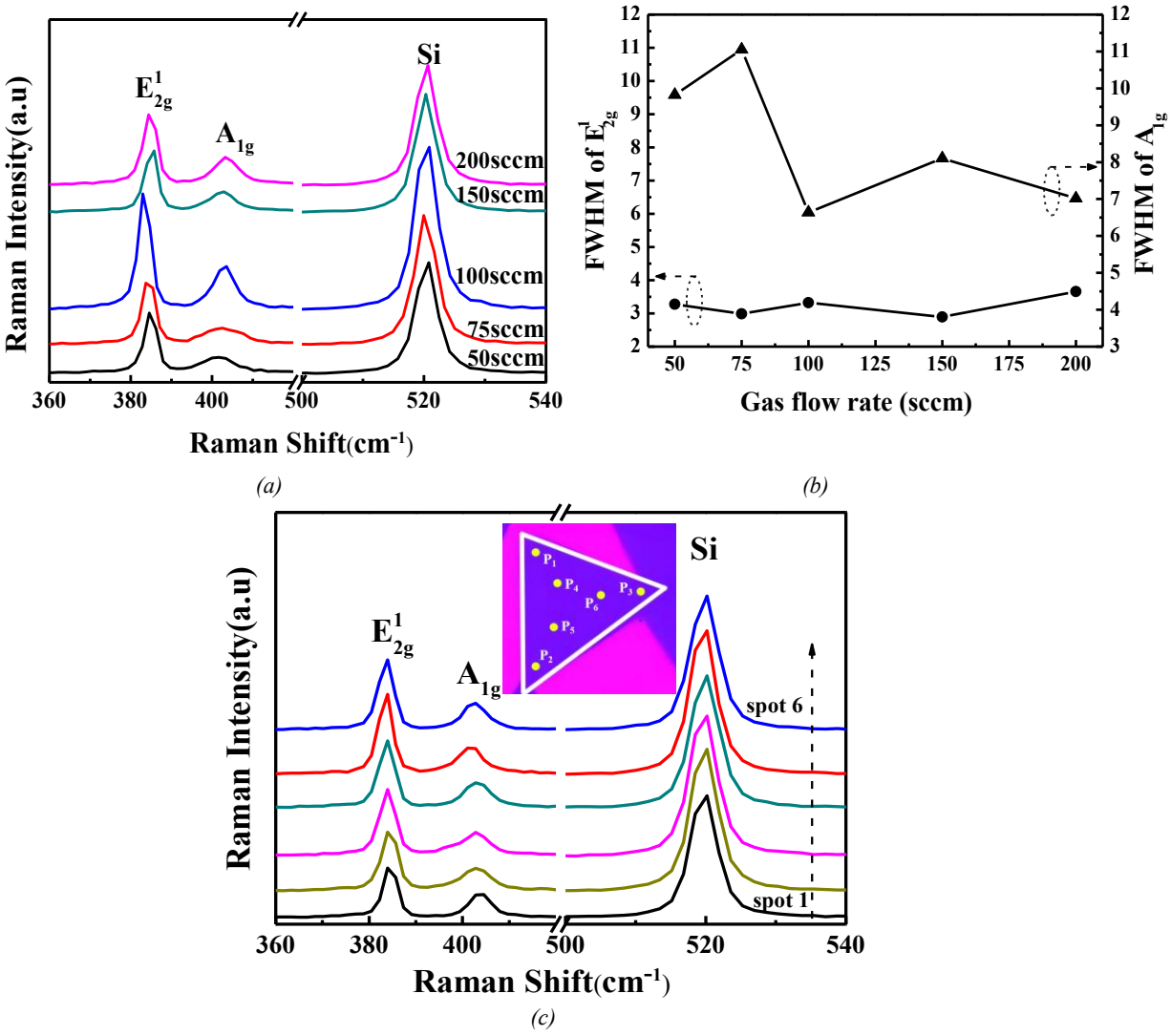

Fig. 3. (a) Raman spectrum of as-grown MoS_2 nanosheets with different carrier gas flow rates; (b) The FWHM of E^1_{2g} and A_{1g} vibration mode; (c) Raman spectra collected from different spots of the MoS_2 nanosheet enclosed by a white triangle in Fig. 2(b) (colour online)

The Raman vibrational modes, wavenumber difference and E^1_{2g}/A_{1g} peak intensity ratio for as-grown MoS_2 nanosheets under various carrier gas flow rates are shown in Table 1. It can be seen that although there are some differences in the location of E^1_{2g} and A_{1g} peaks of MoS_2 nanosheets grown by various flow rates, the wavenumber difference between two characteristic Raman peaks is in the range of 16.7~19.7 cm^{-1} for all samples. This value is in accordance well with the reported value for CVD-grown monolayer MoS_2 [33, 34]. Therefore, the result indicates that all as-grown MoS_2 nanosheets under different flow rates are monolayer. To confirm the uniformity of the thickness of as-grown MoS_2 nanosheets, the Raman spectra (as shown in Fig. 3(c)) were collected from random six spots in the triangular MoS_2 nanosheet enclosed by a white triangle in Fig. 2(b). The consistent

Raman spectral profiles and the wavenumber difference values of approximately 18.5cm^{-1} indicate the as-grown MoS_2 is a monolayer with uniform thickness. In other words, the carrier gas flow rate has little or no effect on the thickness of MoS_2. Moreover, the full width at half maximum (FWHM) of E^1_{2g} and A_{1g} may be used to evaluate the crystalline quality and doping level or binding force between different layers of as-grown MoS_2 nanosheets, respectively. As shown in Fig. 3b, the FWHM of E^1_{2g} peak is in the range of 2.90~3.66 cm^{-1} which is in good agreement with the reported value for mechanically exfoliated monolayer MoS_2 [35, 36], suggesting that all the MoS_2 nanosheets synthesized by different flow rate have good crystalline quality. Whereas, the FWHM of A_{1g} peak fluctuates greatly in the range from 6.64 to 11.05 cm^{-1}, which is related to the difference in binding force between layers or doping level [31, 34]. The FWHM of A_{1g} peak of MoS_2 nanosheets under a higher flow rate (≥100sccm) is lower than the other samples grown at a lower flow rate (<100sccm), which illustrates that high purity MoS_2 nanosheets with low doping level can be obtained at a higher flow rate. To summarize, the carrier gas flow rate has little effect on the thickness of MoS_2 nanosheets, but can effectively modulate doping level.

Table 1. Summary of the E^1_{2g} and A_{1g} peak frequencies and the wavenumber difference between the E^1_{2g} and A_{1g} peak for MoS_2 nanosheets grown by various flow rates.

Carrier gas flow rate (sccm)	E^1_{2g} peak frequency (cm^{-1})	A_{1g} peak frequency (cm^{-1})	The wavenumber difference between E^1_{2g} and A_{1g}(cm^{-1})	E^1_{2g}/ A_{1g} peak intensity ratio
50	385	401.7	16.7	3.98
75	384.5	402.9	18.4	4.64
100	383.4	403.1	19.7	2.83
150	385.1	402.6	17.5	3.67
200	384.8	403.6	18.8	2.74

3.3. PL spectra

As is well known, monolayer MoS_2 is a direct gap semiconductor with a band gap energy of 1.8~1.9 eV and exhibits strong intense PL spectra [1]. Fig. 4 shows the photoluminescence spectra of MoS_2 nanosheets grown at different flow rates. There are two emission peaks A and B, originating from direct exciton transitions between the maximal splitting valence bands and the minimum of the conduction band [2,37]. Emission peaks A and B are located at 1.78~1.83eV and 1.94~1.99eV, respectively. Emission peak B is located about 150meV above emission peak A (Fig. 4b). This result is similar to that of exfoliated monolayer MoS_2 and demonstrates the monolayer thickness of as-grown MoS_2 nanosheets [1]. It is worth noting that the large differences in transition energy between MoS_2 synthesized on a SiO_2/Si substrate (≈1.82eV) and the freestanding single-layer MoS_2 (1.90eV) may be attributed to n-type doping of the MoS_2 due to charge-transfer effects from the substrate [38, 39]. All MoS_2 nanosheets grown at different flow rates show a similar spectral profile in terms of peak position except the sample for 75sccm. As for the MoS_2 nanosheets synthesized at the flow rate of 75sccm, only emission peak A can be observed while without B in the PL spectrum, which are analogous to the freestanding monolayer MoS_2 with low n-type doping density, indicating that the samples grown at 75sccm with low defect density and high crystalline quality [38].

The FWHM of emission peaks A and B is shown in Fig. 4c. From the figure, we can see that the FWHM of A peak and B peak for gas flow rate of 75sccm and 100sccm are found to be narrower than those for other flow rates. The result suggests high crystalline quality MoS_2 nanosheets can be grown at an appropriate gas flow rate (75~100sccm), which is coincident well with Raman analysis [1]. For this reason, the carrier gas flow rate is a vital parameter for the crystalline quality of as-grown MoS_2 nanosheets.

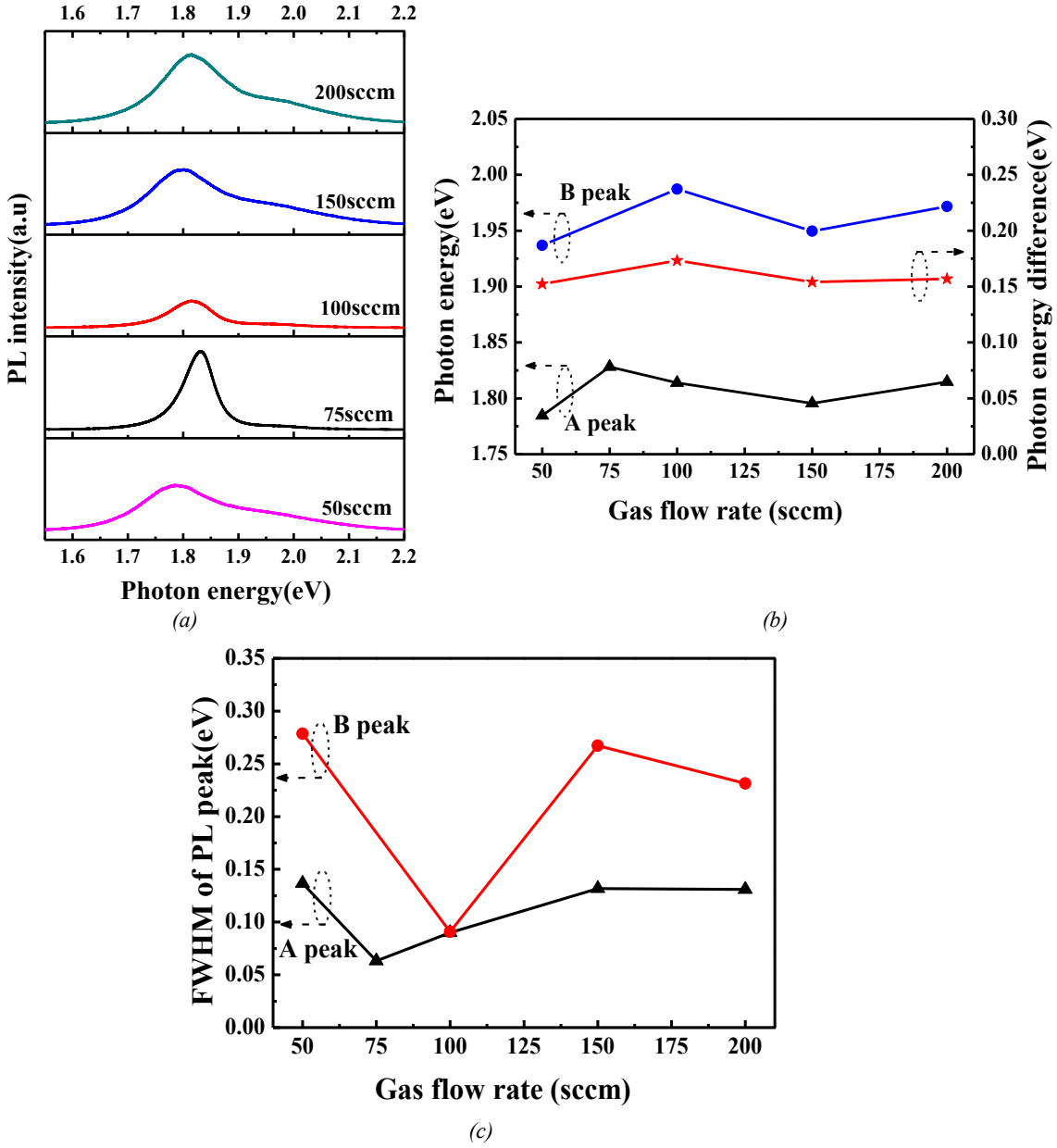

Fig. 4. (a) Photoluminescence spectra of as-grown MoS_2 nanosheets with different carrier gas flow rates. (b) The locations of main peaks and its photon energy difference with respect to carrier gas flow rate. (c) The FWHM of A and B peaks (colour online)

4. Conclusions

We demonstrated a CVD synthesis of monolayer MoS_2 nanosheets at different carrier gas flow rates. The optical images, Raman and PL spectra show that the morphology, coverage, side length, crystalline quality and optical properties of as-grown MoS_2 nanosheets can be tunable by means of control of carrier gas flow rate. The large triangular monolayer MoS_2 nanosheets with high crystalline quality and excellent optoelectrical property were obtained under an appropriate flow rate of 75sccm. The results suggest that the carrier gas flow is a crucial factor for the growth of high-quality triangular monolayer MoS_2 nanosheets.

Acknowledgments

This project has been supported by the key Scientific Research Foundation of Anhui Provincial Education Department (Grant No. KJ2019A0575, KJ2021A0639).

References

[1] K. F. Mak, C. Lee, J. Hone, J. Shan, T. F. Heinz, Physical Review Letters **105**, 136805 (2010).
[2] A. Splendiani, L. Sun, Y. Zhang, T. Li, J. Kim, C. Y. Chim, G. Galli, F. Wang, Nano Letters **10**, 1271 (2010).
[3] R. S. Sundaram, M. Engel, A. Lombardo, R. Krupke,

A. C. Ferrari, Ph. Avouris, M. Steiner, Nano Letters **13**, 1416 (2013).
[4] I. H. Abidi, S. P. Giridhar, J. O. Tollerud, J. Limb, M. Waqar, A. Mazumder, E. L. Mayes, B. J. Murdoch, C. Xu, A. Bhoriya, A. Ranjan, T. Ahmed, Y. Li, J. A. Davis, C. L. Bentley, S. P. Russo, E. D. Gaspera, S. Walia, Advanced Functional Materials **34**, 2402402 (2024).
[5] L. Zou, D. Sang, S. Ge, Y. Yao, G. Wang, X. Wang, J. Fan, Q. Wang, Journal of Alloys and Compounds **972**, 172819 (2024).
[6] B. Radatović, O. Çakıroğlu, V. Jadriško, R. Frisenda, A. Senkić, N. Vujičić, M. Kralj, M. Petrović, A. Castellanos-Gomez, ACS Applied Materials and Interfaces **16**, 15596 (2024).
[7] S. Li, F. Wang, Y. Wang, J. Yang, X. Wang, X. Zhan, J. He, Z. Wang, Advanced Materials **36**, 2301472 (2024).
[8] X. Lin, X. Huang, Q. Zhang, J. Yi, S. Liu, Q. Liang, Applied Physics Letters **123**, 180501 (2023).
[9] M. Mohan, N. P. Shetti, T. M. Aminabhavi, Materials Today Chemistry **27**, 101333 (2023).
[10] T. Van Nguyen, M. Tekalgne, T. P. Nguyen, Q. Van Le, S. H. Ahn, S. Y. Kim, Battery Energy **2**, 20220057 (2023).
[11] T. X. Huang, X. Cong, S. S. Wu, J. B. Wu, Y. F. Bao, M. F. Cao, L. Wu, M. L. Lin, X. Wang, P. H. Tan, B. Ren, Nature Catalysis **7**, 646 (2024).
[12] Y. Jia, Y. Zhang, H. Xu, J. Li, M. Gao, X. Yang, ACS Catalysis **14**, 4601 (2024).
[13] M. A. Islam, P. Serles, B. Kumral, P. G. Demingos, T. Qureshi, A. Meiyazhagan, A. B. Puthirath, M. S. B. Abdullah, S. R. Faysal, P. M. Ajayan, D. Panesar, C. V. Singh, T. Filleter, Applied Physics Reviews **9**, 041301 (2022).
[14] Q. Wu, C. Wang, Q. Xu, X. Zhang, Z. Cai, L. Lin, X. Gu, K. Ostrikov, H. Nan, S. Xiao, Vacuum **216**, 112489 (2023).
[15] A. Ansh, U. Patbhaje, J. Kumar, A. Meersha, M. Shrivastava, Communications Materials **4**, 8 (2023).
[16] S. Li, D. Ouyang, N. Zhang, Y. Zhang, A. Murthy, Y. Li, S. Liu, T. Zhai, Advanced Materials **35**, 2211855 (2023).
[17] K. Y. Yang, H. T. Nguyen, Y. M. Tsao, S. B. Artemkina, V. E. Fedorov, C. W. Huang, H. C. Wang, Scientific Reports **13**, 8378 (2023).
[18] J. Li, S. Wang, Q. Jiang, H. Qian, S. Hu, H. Kang, C. Chen, X. Zhan, A. Yu, S. Zhao, Y. Zhang, Z. Chen, Y. Sui, S. Qiao, G. Yu, S. Peng, Z. Jin, X. Liu, Small **17**, 2100743 (2021).
[19] J. S. H. Deijkers, A. A. de Jong, M. J. Mattinen, J. J. P. M. Schulpen, M. A. Verheijen, H. Sprey, J. W. Maes, W. E. M. M. Kessels, A. A. Bol, A. J. M. Mackus, Advanced Materials Interfaces **10**, 2202426 (2023).
[20] X. Zheng, Y. Zhu, Y. Sun, Q. Jiao, Journal of Power Sources **395**, 318 (2018).
[21] U.Patra, F. Mujeeb, J. Israni, S. Dha, Surfaces and Interfaces **58**, 105825 (2025).
[22] M. Faiha, M. Vikram, S. Arushi, K. Mansi, C. Arindam, S. Alok, D. Subhabrata, Applied Physics Letters **125**, 213103 (2024).
[23] Y. Xia, X. Chen, J. Wei, S. Wang, S. Chen, S. Wu, M. Ji, Z. Sun, Z. Xu, W. Bao, P. Zhou, Nature Materials **22**, 1324 (2023).
[24] P. P. Tummala, C. Martella, A. Molle, A. Lamperti, Nanomaterials **12**, 973 (2022).
[25] V. T. Nguyen, S. Ha, D. I. Yeom, Y. H. Ahn, S. Lee, J. Y. Park, Current Applied Physics **19**, 1127 (2019).
[26] Z. Zhu, S. Zhan, J. Zhang, G. Jiang, M. Yi, J. Wen, Materials Research Express **6**, 095011 (2019).
[27] H. Liu, Y. Zhu, Q. Meng, X. Lu, S. Kong, Z. Huang, P. Jiang, X. Bao, Nano Research **10**, 643 (2017).
[28] S. Ganorkar, J. Kim, Y. H. Kim, S. I. Kim, Journal of Physics and Chemistry of Solids **87**, 32 (2015).
[29] Y. Cao, X. Luo, S. Han, C. Yuan, Y. Yang, Q. Li, T. Yu, S. Ye, Chemical Physics Letters **631**, 30(2015).
[30] F. Esposito, M. Bosi, G. Attolini, F. Rossi, R. Fornari, F. Fabbri, L. Seravalli, Nanomaterials **14**, 1749 (2024).
[31] B. Chakraborty, A. Bera, D. V. S. Muthu, S. Bhowmick, U. V. Waghmare, A. K. Sood, Physical Review B **85**, 161403 (2012).
[32] M. R. Laskar, L. Ma, S. Kannappan, P. S. Park, S. Krishnamoorthy, D. N. Nath, W. Lu, Y. Wu, S. Rajan, Applied Physics Letters **102**, 252108 (2013).
[33] S. L. Li, H. Miyazaki, H. Song, H. Kuramochi, S. Nakaharai, K. Tsukagoshi, ACS Nano **6**, 7381 (2012).
[34] C. Lee, H. Yan, L. E. Brus, T. F. Heinz, J. Hone, S. Ryu, ACS Nano **4**, 2695 (2010).
[35] K. K. Liu, W. Zhang, Y. H. Lee, Y. C. Lin, M. T. Chang, C. Y. Su, C. S. Chang, H. Li, Y. Shi, H. Zhang, C. S. Lai, L. J. Li, Nano Letters **12**, 1538 (2012).
[36] Y. Yu, C. Li, Y. Liu, L. Su, Y. Zhang, L. Cao, Scientific Reports **3**, 1866 (2013).
[37] P. Tonndorf, R. Schmidt, P. Böttger, X. Zhang, J. Börner, A. Liebig, M. Albrecht, C. Kloc, O. Gordan, D. R. T. Zahn, S. M. de Vasconcellos, R. Bratschitsch, Optics Express **21**, 4908 (2013).
[38] X. Zhang, H. Nan, S. Xiao, X. Wan, Z. Ni, X. Gu, K. Ostrikov, ACS Applied Materials and Interfaces **9**, 42121 (2017).
[39] N. Scheuschner, O. Ochedowski, A. M. Kaulitz, R. Gillen, M. Schleberger, J. Maultzsch, Physical Review B **89**, 125406 (2014).

*Corresponding author: zszhu@aqnu.edu.cn